Global Distribution of Asian, Middle Eastern, and North African Dust Simulated by CESM1/CARMA

Siying Lian[1], Luxi Zhou[2], Daniel M. Murphy[3], Karl D. Froyd[3], Owen B. Toon[4], and Pengfei Yu[1*]

[1]Institute for Environmental and Climate Research, Jinan University, Guangzhou, China

[2]Guangzhou Institute of Tropical and Marine Meteorology, CMA, Guangzhou, China

[3]Chemical Science Laboratory, National Oceanic and Atmospheric Administration, Boulder, Colorado

[4]Department of Atmospheric and Oceanic Sciences and Laboratory for Atmospheric and Space Physics, University of Colorado, Boulder, Colorado

Corresponding author: Pengfei Yu (pengfei.yu@colorado.edu)

Abstract.

Dust aerosols affect the radiative and energy balance at local and global scales by scattering and absorbing sunlight and infrared light. Previous study suggests dust size distribution is one of the major sources of uncertainty in modelling the dust global distribution. Climate models overestimates the fine dust ($\leq$ 5 μm) by an order of magnitude, while underestimates the coarse dust ($\geq$5μm) ranges between half to one-and-a-half orders of magnitude compared with the global observations. Here we improved the simulated size distribution of dust aerosol using a sectional aerosol model coupled with the Community Earth System Model (CESM1/CARMA). Simulated dust mass size distributions peak at around 2-3 micrometers in diameter and increase by 4 orders of magnitude from 0.1 μm to 2 μm. Our model demonstrates that North African, Middle Eastern, and Asian dust accounts for ~59.7%, 12.5%, and 13.3% to the global annual mean dust emissions, with the remaining 14.5% originating from scattered smaller dust sources. The model dust vertical distributions are validated against the NASA Atmospheric Tomography (ATom) field campaign datasets. Both simulations and ATom in-situ measurements during ATom field campaign suggest that dust mass concentrations over the remote ocean drop by two to three orders of magnitude from the surface to the upper troposphere (200 hPa). Our model suggests that Asian dust contributes to more than 40% of annual mean dust mass abundances in the global upper troposphere and lower stratosphere (UTLS). Model suggests that the Asian dust dominates the dust mass budget in the UTLS of the Asian summer monsoon (ASM) region, with a relative contribution 1-2 orders of magnitude higher than the dust originated from North African and Middle Eastern deserts.

1 Introduction

Mineral dust, from both natural and anthropogenic sources, accounting for more than 50% of the total global aerosol mass burden (Textor et al., 2006; Andreae, 1995; Andreae et al., 1986; Zender et al., 2004). Mineral dust impacts the radiation balance of the planet by scattering and absorbing sunlight, and unlike most other types of aerosols, dust has significant effects on thermal radiation due to its relatively large particle sizes (i.e., Satheesh and Moorthy, 2005; Sokolik and Toon, 1996; Balkanski et al., 2007; Tegen and Lacis, 1996). Dust optical properties vary between different sources (Sokolik and Toon, 1999), making it complex to construct global models of dust radiative effects. Dust also indirectly impacts climate by serving as a prominent nuclei for heterogenous ice formation (e.g., Maloney et al., 2022; Cziczo et al., 2013). Despite being insoluble, dust can also serve as cloud condensation nuclei due to the large particle sizes of dust, influencing cloud microphysical and rainfall processes (Rosenfeld et al., 2001; Levin et al., 1996).

Tegen and Schepanski (2009) suggest that the Sahara and Asia are the largest source regions of mineral dust on Earth, accounting for more than 60-95% of the global dust load. Saharan dust is lifted all year, primarily due to subtropical weather systems. Saharan dust can travel across the Atlantic Ocean, driven by the trade wind circulation (Karyampudi, 1979; Karyampudi et al., 1999). Asian dust is mostly lifted in the spring by mid-latitude frontal systems, and is likely to be removed near its source due to rainfall though it can be carried at upper levels across the Pacific (Su and Toon, 2011). The North African and Asian dust can be transported to the upper troposphere (UT) and even farther around the Earth by subtropical westerly jets (Yang et al., 2022).

The accurate representation of the dust emissions from individual source regions is important to understand the climate impact of dust on the Earth system (Kok et al., 2021). The contributions of dust from the different source regions to the global dust load are still uncertain. Global model simulations show that the dust emission from different sources regions differ by an order of magnitude among different models (Huneeus et al., 2011).

One source of uncertainty in quantify the emission of dust aerosols that can be attributed to the size distribution of dust aerosol (Tegen, 2003). The emitted dust size distribution is a basic parameter to simulate (Huneeus et al., 2011) and the lifetime and radiative of dust with different particle sizes differ substantially that impact the simulation of dust on global scale (Kok, 2011). Kok (2011) showed

64 that most Global Climate Models (GCM) overestimate the dust emitted fraction with particle size less

65 than 2 µm by a factor of ~2-8 and underestimate the fraction of emitted with greater than 5 µm which

66 causes the underestimation of dust global emission rate.

67   The vertical distribution of dust are crucial for understanding the vertical and long-distance

68 transport of dust aerosols. Bourgeois et al. (2015) showed that the residence time of dust is

69 significantly affected by its vertical location during long-range transport. However, in-situ

70 measurements of dust's vertical distribution from the surface to the upper troposphere are extremely

71 limited compared with surface measurements. Yu et al. (2015a) calculated the vertical mass flux of

72 dust by converting the dust extinction coefficient of CALIOP to dust mass concentration, yielding

73 estimated dust mass fluxes with an uncertainty of $\pm$ (45-70%). Yu et al. (2010) showed that the

74 modeled dust extinction of GOCART exceeded CALIOP's measurements by more than a factor of two

75 from the middle to the upper troposphere over the northwestern Pacific. Based on CloudSat satellite

76 data from 2007 to 2009 combined with CALIOP/CPR nighttime measurements, Yang et al. (2022)

77 suggested that the dust mass loading at 4-10 km in the Northern Hemisphere (NH) reaches a maximum

78 in March-April-May. The dust concentrations in 4-6 km have an opposite phase with the wind speed

79 over Africa and West Asia. Despite the great coverage of satellite data, remote sensing techniques have

80 considerable uncertainty in retrieving the dust vertical distribution. From 2016-2018, a pole-to-pole

81 airborne in-situ measurement from NASA Atmospheric Tomography Mission (ATom) field campaign

82 (Froyd et al., 2022; Wofsy et al., 2018) in-situ measured dust vertical distributions from pole to pole

83 and from surface to the upper troposphere over the remote ocean.

84   Dust aerosol can be transported to the upper troposphere (UT) via the deep convections. Dust

85 transported to the upper troposphere can affect cirrus formation through heterogeneous nucleation (???;

86 Froyd et al., 2022). Ma et al. (2019) simulated the chemical composition of Asian tropopause aerosol

87 layer and found a dust maximum inside the anticyclone of Asian Summer Monsoon (ASM). However,

88 the abundance, source attributions, and spatial-temporal distribution of dust in the UT of ASM are still

89 of large uncertainties.

90   We use a sectional aerosol model coupled with a climate model to study the global distribution of

91 dust, with a focus on the size distribution and vertical distribution. We compare the simulated dust

92 abundance from the surface to the upper troposphere with in-situ measurements from ATom field

93 campaign (Froyd et al., 2022). Then we use the constrained model to simulate the spatiotemporal

94   distribution of dust coming from the Sahara, Middle East, and East Asia. Finally, we estimate dust

95   source attributions during the Asian summer monsoon from the three source regions.

96   **2   Methods**

97   **2.1 CESM1/CARMA model**

98   We use a sectional aerosol microphysics model, the Community Aerosol and Radiation Model for

99   Atmospheres (CARMA) (Yu et al., 2015b; Yu et al., 2019; Bardeen et al., 2008; Toon et al., 1988)

100   coupled with the NSF/DOE Community Earth System Model (CESM) to simulate the global

101   distribution of dust between 2014 and 2019. The model simulations are conducted at a horizontal

102   resolution of 1.9°×2.5° and with a time step of 30 min. The model has 56 hybrid levels from the surface

103   up to about 45 km, with a vertical resolution of about 1 km near the tropopause. The meteorological

104   fields were nudged to Goddard Earth Observing System (GEOS5) reanalysis data.

105   CESM1/CARMA includes two groups of particles. The first group is liquid sulfuric acid droplets

106   that form from gas phase nucleation and span a diameter range from 0.2 nm to 2.6 μm. The second

107   group is an internal mixture of primary emitted organics, secondary organics, dust, sea salt, black

108   carbon, and condensed sulfate (Yu et al., 2015b). The mixed particles are resolved with 20 discrete size

109   bins with diameters ranging from 100 nm to 17 μm in the model. The aerosol optical properties in

110   CESM1/CARMA are estimated using a Mie scattering code, with inputs based on particle size, relative

111   humidity, and aerosol composition (Yu et al., 2015b). We assume that dust has a density of 2.65 g/cm^3

112   and use wavelength dependent refractive indices (RI) (Yu et al., 2015b). The RI at 532 nm is 1.53-

113   0.006i in the mode, which is independent of the dust source region, even though these properties vary

114   with dust source in reality. Note that the reported imaginary part of the refractive index of dust aerosol

115   ranges from 0.0006 to 0.0048 according to previous studies (Sinyuk et al., 2003; Di Biagio et al., 2019;

116   Balkanski et al., 2007), which suggests that our model may overestimates the absorption aerosol optical

117   depth from dust aerosol.

118   **2.2 Dust emission parameterization**

119   Mineral dust emission is simulated as a saltation-sandblasting process, which can be explained by the

120   wind erosion theory. The process is driven by surface stress, which is usually expressed as friction wind

121   velocity (Ginoux et al., 2001). When the frictional wind speed exceeds a certain threshold, the force of

122 the wind will overcome the gravitational force of the sand grains and the cohesive forces between

123 particles, and sand-sized particles will saltate. When they impact the surface dust particles will be

124 lofted into the air (Marticorena and Bergametti, 1995). The wind-driven emission of dust aerosols in

125 CESM1/CARMA is provided by Su and Toon (2009) and Yu et al. (2015b). The total emission flux is

126 parameterized as:

127
$$F_{total} = C \times S_e \times (u - u_t) \times u^2,$$

128 where F_{total} is the particle size dependent flux of dust; C is an arbitrary constant that depends on

129 the spatial resolution of the climate model among other factors and is set to 0.6 $\mu g\ s^2 m^{-5}$; u is the 10-

130 m wind speed, which is parameterized by the surface friction velocity (u^*) and the 10-m drag

131 coefficient (C_d) so that under neutral conditions $u = \frac{u^*}{\sqrt{C_d}}$; and u_t is the threshold wind speed, which

132 depends on the particle size (Su and Toon, 2009; Marticorena and Bergametti, 1995). Details on u^*, u_t ,

133 and C_d can be found in Yu et al. (2015b). S_e is the dust erodibility factor, which denotes the efficiency

134 of dust lifting and derived from the TOMS aerosol index reported by Ginoux et al. (2001).

135 Following Prospero and Bonatti (1969), the model assumes that 90% of the dust emission mass

136 flux is distributed in silt bins with diameter ranges from 2.6 to 17.4 µm, and the remaining 10% is in

137 clay bins with diameter ranges from 0.1 to 2 µm (Yu et al., 2015b). In the present study, we adjust the

138 relative mass fractions in clay and silt bins to match the data reported by Adebiyi and Kok (2020) and

139 discussed in section 3.1 below.

140 **2.3 Convective transport parameterization**

141 Particles are primarily activated at the cloud base. CESM1/CARMA considers the activation of

142 particles, including dust, from the entrained air above the cloud bases (secondary activation, Froyd et

143 al., 2022; Yu et al., 2019). Previous studies have found that climate models that fail to consider

144 secondary activation above the cloud base overestimate the abundance of primary particles like sea salt

145 and black carbon in the upper troposphere by orders of magnitude (Yu et al., 2019; Murphy et al.,

146 2021). A comparison with global airborne measurements of dust suggests that dust is also subject to

147 secondary activation above the cloud base and subsequent in-cloud removal (Froyd et al., 2022). For

148 below-cloud scavenging, the tunning parameter for aerosol's solubility in CESM1/CARMA is 0.2 for

149 dust and 1.0 for sea salt (Yu et al., 2015b). For convective removal, we treat dust's removal efficiency

150 the same as other aerosol types. Details of the parameterizations can be found in Wang et al. (2013),

151   Grell and Freitas (2014), and the supplement of Yu et al. (2019).

2.4 ATom airborne field campaign

153   The Atmospheric Tomography Mission (ATom) was an airborne field campaign with in-situ

154   measurements of atmospheric composition in the remote troposphere from about 0.18 to 12 km in

155   altitude in the Pacific and Atlantic basins, spanning from ~82°N to ~86°S latitude (Spanu et al., 2020;

156   Wofsy et al., 2018). It consisted of 48 science flights by the NASA DC-8 aircraft with 548 vertical

157   profiles during four flight series covering roughly the same loop (Bourgeois et al., 2020). A

158   comprehensive set of aerosol measurement data including mineral dust was collected from July 2016 to

159   May 2018.

160   In this study we compare the simulations with measured dust concentrations during the ATom

161   mission from 2016 to 2018. Dust concentration data are based on data from the National Oceanic and

162   Atmospheric Administration (NOAA) Particle Analysis by Laser Mass Spectrometry (PALMS)

163   instrument (Froyd et al., 2019; Brock et al., 2019; Murphy et al., 2003). The PALMS instrument measures

164   the chemical composition of individual ambient particles from about 0.1 to 4.8 μm in diameter by

165   evaporating individual particles and then using a time of flight mass spectrometer to analyze ions

166   (Murphy et al., 2006). Dust and other particle types are classified using spectral signatures. Dust mass

167   concentrations are then determined by combining the PALMS classifications with absolute particle

168   concentrations from independent optical particle counters (Froyd et al., 2019; Froyd et al., 2022). The

169   measured aerodynamic particle size are converted to the geometric diameter using a constant density and

170   shape factor as described Froyd et al. (2022). To directly compare with ATom dust vertical profiles

171   measured by PALMS, we sample the simulated dust concentration with diameter between 0.1 μm and

172   4.5 μm along the ATom flight track.

2.5 Surface measurement networks

174   Huneeus et al. (2011) summarize dust measurements at the surface around the globe including

175   compiled by Mahowald et al. (2009) and the University of Miami network (Prospero, 1989; Arimoto et

176   al., 1996). Data compiled by Mahowald et al., (2009) contain the data set of short-term measurements

177   from cruises and monitoring stations with daily averaged surface dust concentrations. Cruises measured

178   iron (Fe) and converted to dust by assuming a 3.5% Fe in dust. The iron content in dust varies

179 according to the source regions and this value is the average iron content of the Earth's crust

180 (Mahowald et al., 2005). Long-term observations by the University of Miami include Pacific, Atlantic,

181 and Antarctic Ocean sites globally and measure the mass concentration of dust with diameter less than

182 40 μm (Prospero, 1989, 1996; Arimoto et al., 1996).

3 Model validation

3.1 Dust size distribution and emission

185 Based on global measurements of atmospheric dust size distributions, Adebiyi and Kok (2020) found

186 that the global models in AeroCom (Aerosol Comparison between Observations and Models project)

187 underestimate the coarse dust mass load in the atmosphere by a factor of four and overestimate the fine

188 dust mass load by 1-3 orders of magnitude. Figure 1 shows that CESM1/CARMA Yu et al. (2015b)

189 generally reproduces the measured dust size distribution with diameter less than 1 μm or greater than 3

190 μm within the variabilities of the data. However, the CESM1/CARMA Yu et al. (2015b)

191 underestimates the dust in the size range between 1 and 3 μm by one order of magnitude (red dashed

192 line). In this study, we simply adjust the mass fraction of the emitted dust in the silt bins with geometric

193 diameter greater than 2 μm from 90% to 94%. The global dust size distribution simulated in the

194 modified model (CESM-CARMA solid red line in Fig.1) agrees better with measurements from

195 Adebiyi and Kok (2020) (Figure 1). The simulation show that the model underestimates the coarse-

196 mode dust with diameter larger than 10 μm by ~48%. The modeled total dust concentration at surface

197 can be biased low, while modeled dust in the upper troposphere is not significantly affected as giant

198 dust particles sediments quickly.

199
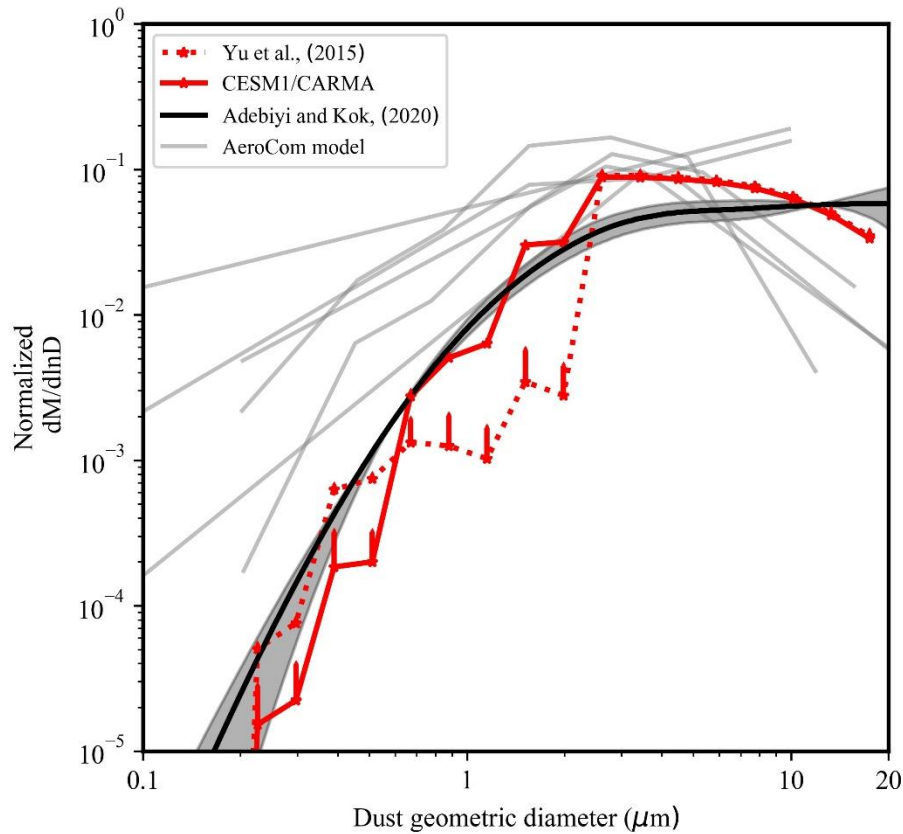
Figure 1. Comparison of the simulated and measured normalized global mean dust size distributions. The dust mass size distributions are divided by the total dust mass integrated over the size range (i.e. the area under each dM/dlnD curve).The global and annual mean dust size distribution simulated by CESM1/CARMA with the dust emission parameterization described in Yu et al. (2015b) is shown by the dashed red line; the simulation by CESM1/CARMA with the modified emission parameterization is shown by the solid red line; temporal variabilities (1 standard deviation) from Yu et al., (2015b) and CESM1/CARMA are denoted by green and cyan lines; the simulated size distribution by the AeroCom models reported in Adebiyi and Kok (2020) is denoted by the gray lines; the measured dust size distribution derived from the global measurements reported in Adebiyi and Kok (2020) is denoted by the solid black line; the shading represent the 95% confidence interval.

210   Figure 2 shows the global annual mean emission of fine (with diameter less than 4.5 μm) and

211   coarse (with diameter greater than 4.5 μm) dust simulated by CESM1/CARMA. The simulated global

212   and annual mean mass emission of coarse dust is higher than that of fine dust by a factor of 2.8. The

213   three largest dust source regions in the world, i.e., the Sahara, Middle East, and Asia contribute ~85%

214   of total global dust emissions, and about 97% of Northern Hemisphere (NH) dust. Dust emissions from

215   the Sahara in North Africa account for ~59.7% of global emissions by mass. Middle Eastern and Asian

216   dust emissions account for ~12.5% and 13.3% of global emissions, respectively.
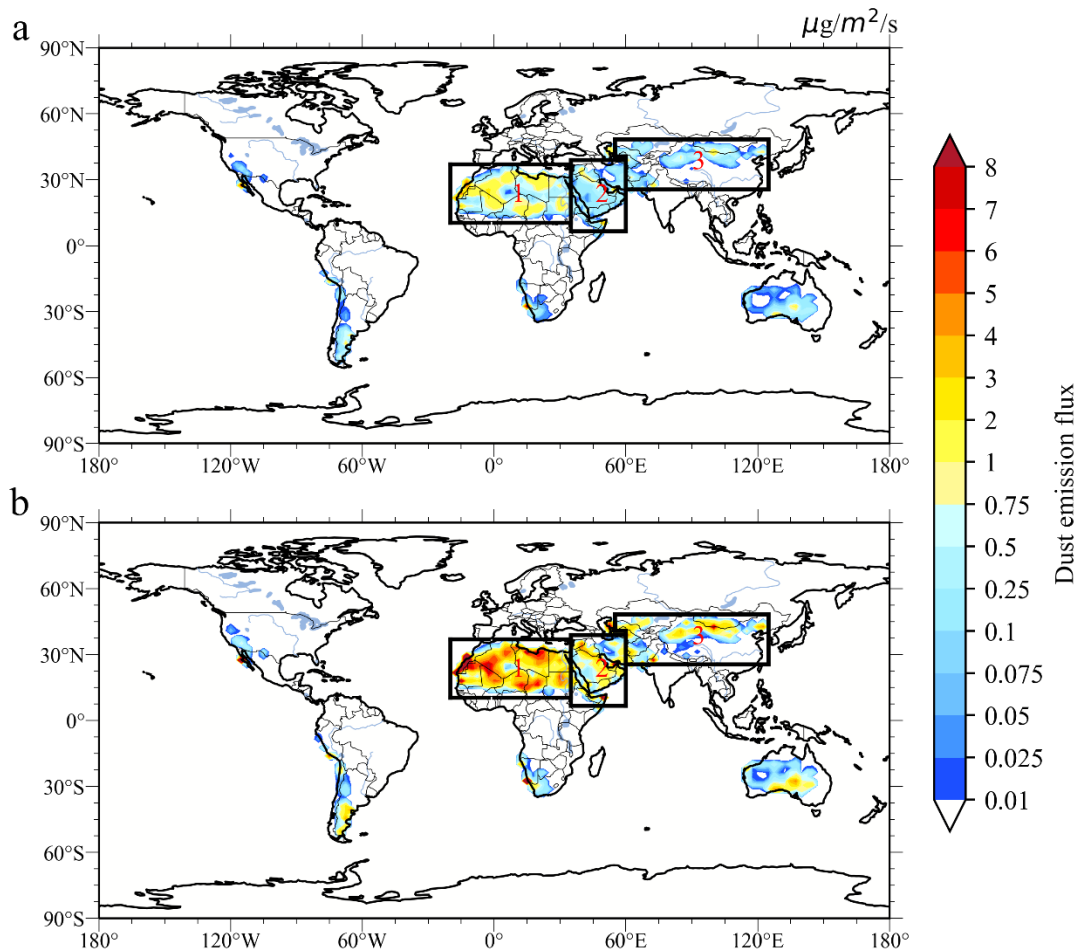
Figure 2. (a) Simulated annual emission flux (μg/m2/s) of dust with geometric diameter less than 4.5 μm in CESM1/CARMA averaged from Feb 2014 to Jan 2018. (b) same as (a) but for dust with geometric diameter larger than 4.5 μm. The regions of interest are denoted by the black boxes. The coordinates of the three regions are (1) North African source (20°W-35°E; 10.4°-36.9°N), (2) Middle Eastern source (35°-60°E; 6.6°-38.8°N), and (3) Asian source (55°-60°E for 40.7°-48.3°N, and 60°-125°E for 25.5°-48.3°N).

3.2 Comparison with dust surface measurements

In Figure 3, we compare the simulated annual mean dust concentrations at the surface from 2014 to 2018 with the observational datasets summarized in Huneeus et al. (2011). In general, the simulated dust concentrations are within one order of magnitude of observations (Figure 3b). The simulated dust underestimated the measured dust concentration from University of Miami network by 70%, while overestimated the dust concentration from the complied dataset (Mahowald et al., 2009) by a factor of 3.75. Both the model and observations show that the dust concentration in the Northern Hemisphere (NH) is about one order of magnitude higher than that in the Southern Hemisphere (SH) due to higher NH dust emissions because of the greater area of Northern Hemisphere (NH) deserts. Because a lack of

233 detailed date information in measurements compiled by Mahowald et al. (2009), the comparison of

234 annual mean model concentration and short-term observations possible result in a large bias but still

235 provide valuable information (Wang et al., 2015). In order to explain the bias, we show the error bars

236 by the median 66 % of the modeled daily averaged model concentration (denoted by the vertical

237 dashed line) for each cruise data following the method suggested by Mahowald et al. (2008) and

238 Huneeus et al. (2011). Near the dust source region (e.g., downwind of the Sahara), the model

239 underestimates the measured median dust surface concentrations by 5.4%. The dust simulation

240 underestimates the averaged ship cruise measurements by 11% over remote ocean basins in the SH.

241 Higher model low biases of 72% are found in the tropical Pacific, which indicates that dust is removed

242 too efficiently amid transport from the source regions.
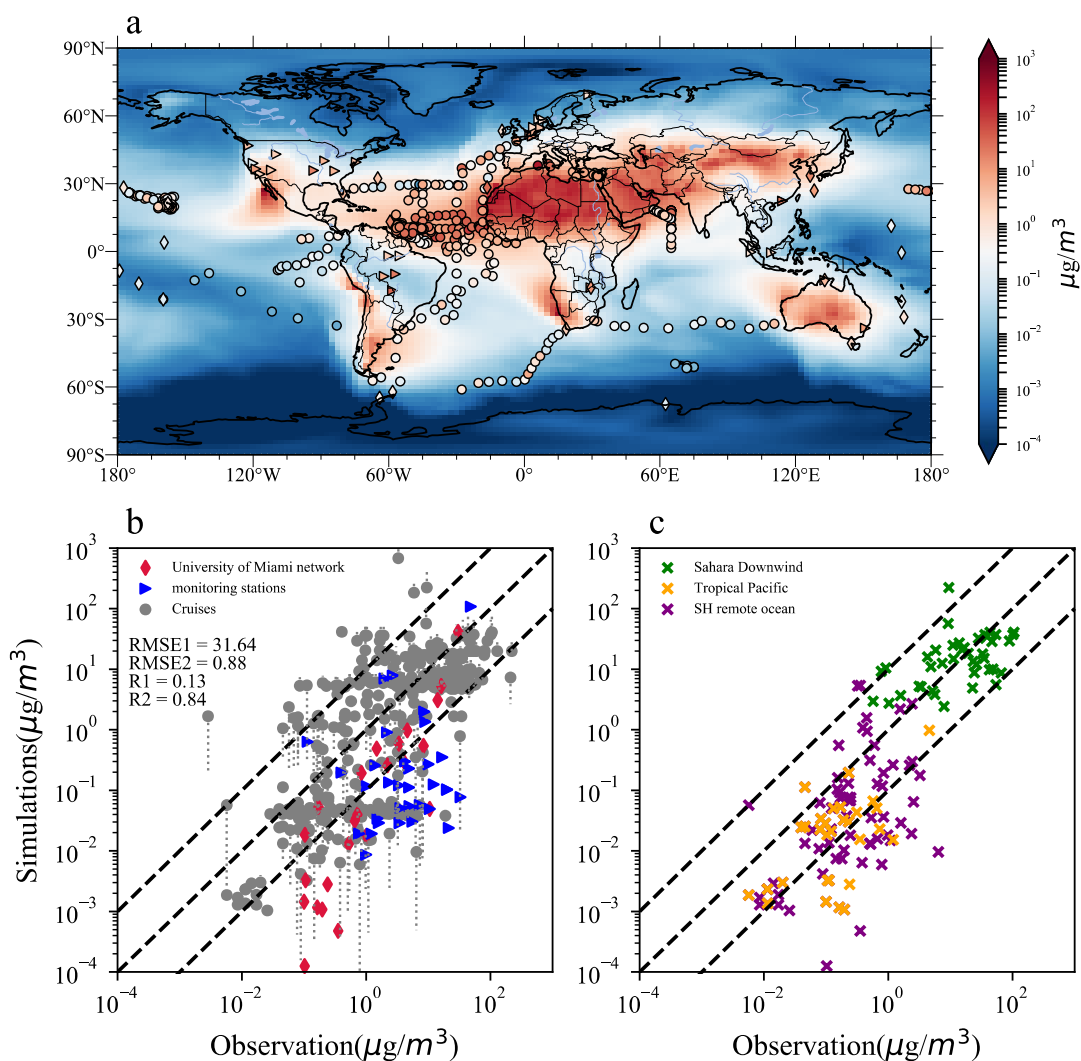
243

244 **Figure 3.** (a) Simulated global dust surface concentrations (μg/m3) averaged from 2014 to 2019 from

245 CESM1/CARMA shown in the filled contour. The summarized dust surface concentration data sets

from Huneeus et al. (2011) are denoted by markers of different shapes. Compiled observations including those from long-term observational sites and cruise data reported in Mahowald et al. (2009) are denoted by triangles and circles, respectively; measurements from the University of Miami network (Prospero 1989; Arimoto et al., 1996) from 1981 to 1998 are denoted by diamonds. (b) Comparison of the simulated dust concentrations by CESM1/CARMA with the compiled observational dataset from Mahowald et al. (2009) and University of Miami network. Gray circles and blue triangles represent selected data from Mahowald et al. (2009) short-term cruises and long-term observations, respectively; red diamonds represent the University of Miami network measurements. "R1" and "RMSE1" represents correlation coefficient (R) and the Root mean square error (RMSE) between simulations and measurements from Mahowald et al., (2009), respectively. In the meantime, "R2" and "RMSE2" denoted the University of Miami dust data. The gray dotted line donated the simulated error bar extracted from the simulated daily concentration following the method in Mahowald et al. (2008). (c) Same as (b), but the North African downwind area as well as the tropical Pacific basin and Southern Hemisphere (SH) remote ocean are represented as green, orange, and purple stars, respectively. The 1:1, 1:10, and 10:1 relationships between the simulated and observed dust concentrations are denoted by the black dashed lines.

Figure 4 compares the simulated concentrations of dust below 1 kilometer above the sea level with diameter less than 4.5 μm near the surface (0-1 km above sea level) over remote ocean basins with the NASA Atmospheric Tomography (ATom1) airborne field campaign (Froyd et al., 2022; Wofsy et al., 2018). Both observations and the model suggest that higher dust concentrations are found in the Atlantic basin downwind of the North African and near the west coast of North America. As shown in Figure 4c, the model underestimates the average dust surface concentrations observed during ATom1 by 62%, with a correlation coefficient of 0.55. Except for the Southern Ocean, the modeled dust concentration is within an order of magnitude of the observations in general. The model strongly underestimates the observed dust concentration in the remote Southern Ocean by over one order of magnitude. The underestimation of southern Pacific Ocean dust could be partly due to underestimation of the emissions in SH. In addition to a possible lack of emissions, the model may generate too much convection and thereby have a too efficient wet scavenging of dust aerosols.
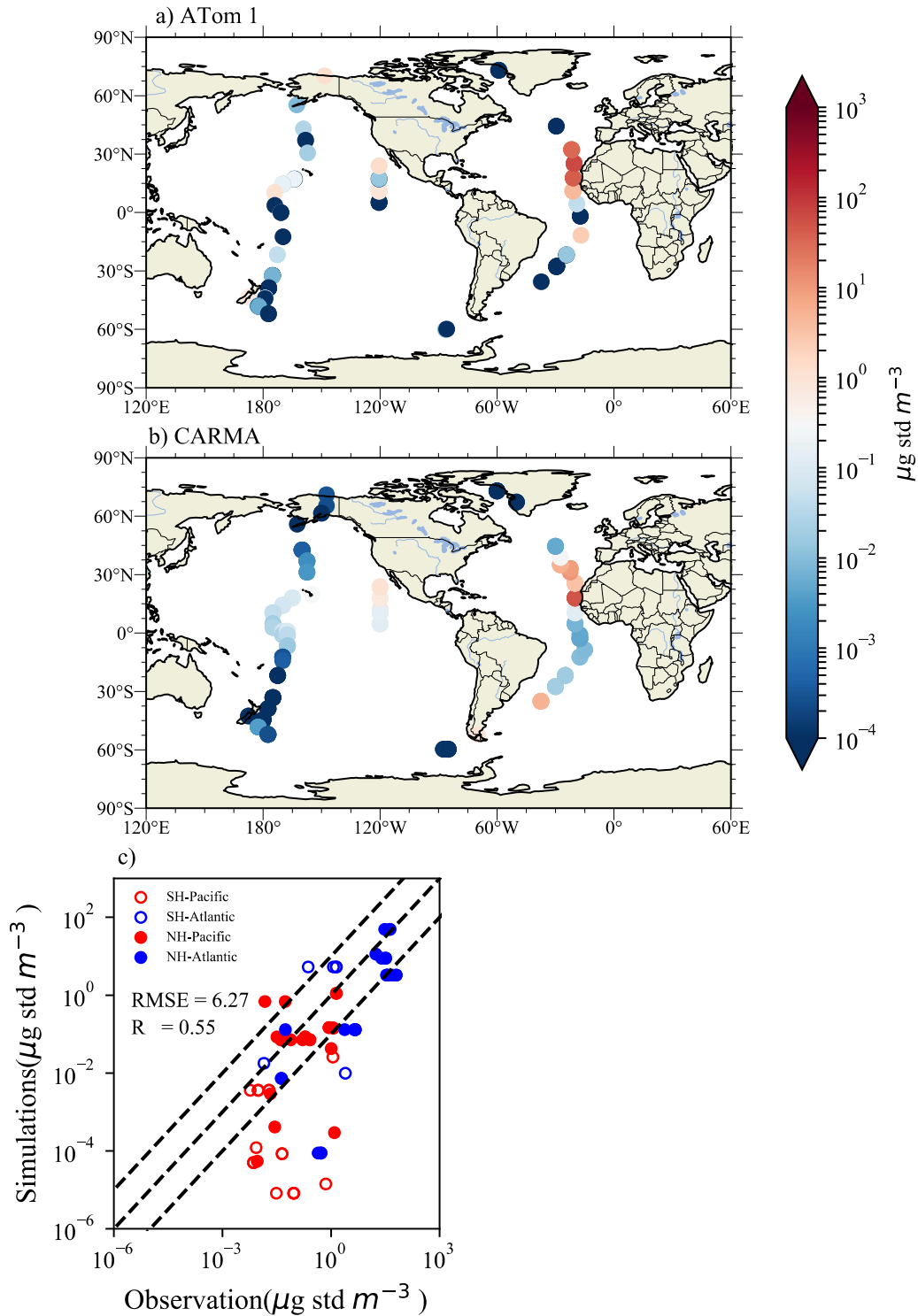
Figure 4. Comparison of the dust concentration below 900 mb with particle diameter less than 4.5 μm simulated by CESM1/CARMA with the NASA ATom 1 airborne campaign. Both model and observations are sampled along the NASA Atom-1 flight track. (a) Observed dust surface concentration according to ATom 1; (b) same as (a), but simulations from CESM1/CARMA. (c) Scatterplot of CARMA simulation compared with ATom 1 for dust surface concentration. Southern Pacific and Atlantic basin sites are denoted by red and blue circles, respectively, while northern Pacific and Atlantic basin sites are denoted by red and blue points, respectively. The black dashed lines in each

282   panel denote 1:10, 1:1, and 10:1 relationships between observations and simulations, respectively.

283   **3.3 Comparison with dust vertical distribution**

284   Figure 5 compares the dust vertical distribution between CESM1/CARMA and measurements by

285   PALMS during ATom1 in August 2016. The observed dust concentrations in the lower tropospheric NH

286   midlatitudes (27ºN-60ºN) and tropics (27ºS-27ºN) are about an order of magnitude higher than those in

287   the SH midlatitudes (27ºS-60ºS) due to higher surface emissions in NH (Figure 2). The tropical lower

288   tropospheric dust loading in the Atlantic basin, which is downwind of the North African, is over one

289   order of magnitude higher than that in the Pacific Ocean. Both observations and the model show that

290   the dust concentration decreases by two to three orders of magnitude from the surface to about 12 km.

291   The strong vertical gradient is consistent with the findings reported in Yu et al. (2019) and Froyd et al.

292   (2022), that deep convection activates the entrained dust aerosols above the cloud base and

293   subsequently removes the particles in-cloud. Maloney et al. (2022) suggests that there is a strong

294   removal of dust by ice formation through heterogeneous nucleation. The model overestimates the

295   observed dust concentration in the mid and upper troposphere possibly because our model does not

296   include the interaction. A layer of dust between 2 and 8 km, which the model fails to reproduce over the

297   southern Atlantic, is observed during ATom1 but not in ATom2-4 (Figure S1-S3). Figure S1 shows that

298   about 35% of the simulated dust near the surface are coarse mode dust (4.5um – 17 um) and the coarse

299   dust mass fraction drops rapidly with altitude. Simulations show that 95% of the total dust

300   concentration above 5 km is fine dust (with diameter less than 4.5 μm) because coarse dust is subject to

301   more efficient wet and dry deposition during long-range transport vertically or horizontally.
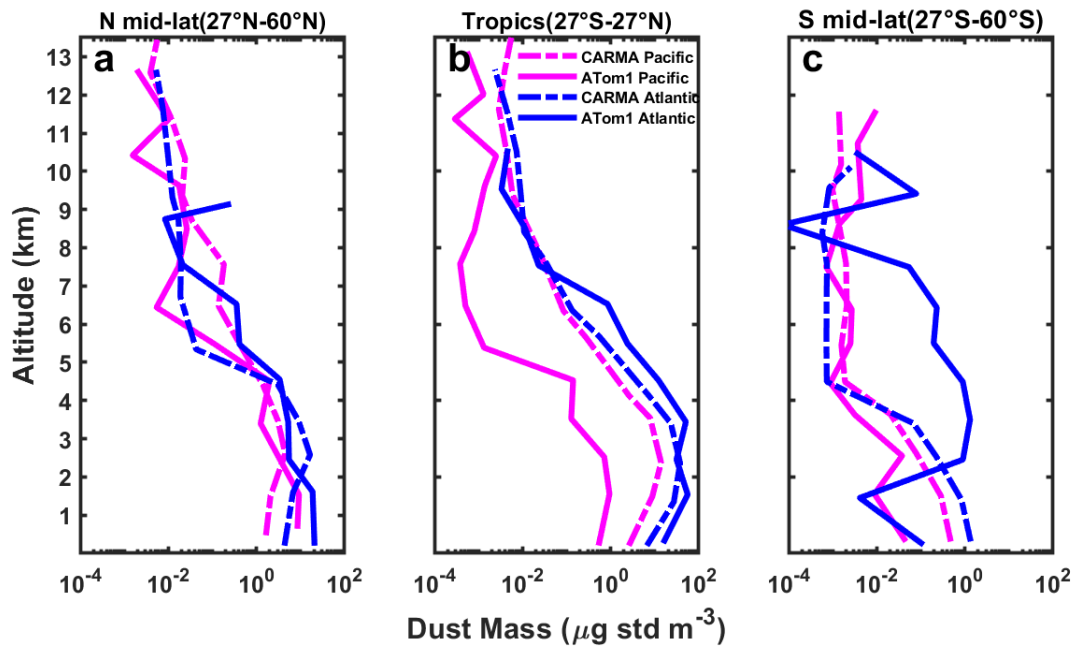
Figure 5. Simulated (long dash line) and measured (solid line) vertical profiles of the dust concentrations during the ATom1 field campaign. Both model and observations are sampled along the flight track. The profiles are averaged over the Pacific Ocean (pink) or Atlantic Ocean (blue) in the Northern Hemisphere (NH) midlatitudes (27ºN-60ºN, panel a) and tropics (27ºS-27ºN, panel b), and in the Southern Hemisphere (SH) midlatitudes (27ºS-60ºS, panel c).

3.4 Comparison with AERONET in Asia and North Africa

The simulated aerosol optical depth (AOD) at 532 nm wavelength from CESM1/CARMA is compared to the measurements near dust source regions from 2014 to 2018 for most of the Aerosol Robotic Network (AERONET) sites (Figure 6a). We use 18 AERONET sites inside of the major dust emission region shown in Figure 2. On average, the model underestimated the annual mean AOD of the selected 18 AERONET sites by 19%. The model underestimates the averaged AOD by ~14% in North Africa and ~25% in Middle East. Figure 6b shows the simulated AOD without dust emitted in the model underestimated the AERONET AOD by 74% on average. The simulations with and without dust emission suggest that dust contribute to over 50% of simulated AOD in the selected AERONET sites. Consistent with the dust emission distribution shown in Figure 2, the simulated and observed AOD near the dust source regions in the tropics and NH (e.g., Sahara, Middle East, and Asia) is significantly higher than that near SH deserts (e.g., central Australia). Dust from the source regions in NH and tropical deserts is transported downwind into the Pacific and Atlantic Ocean basins.
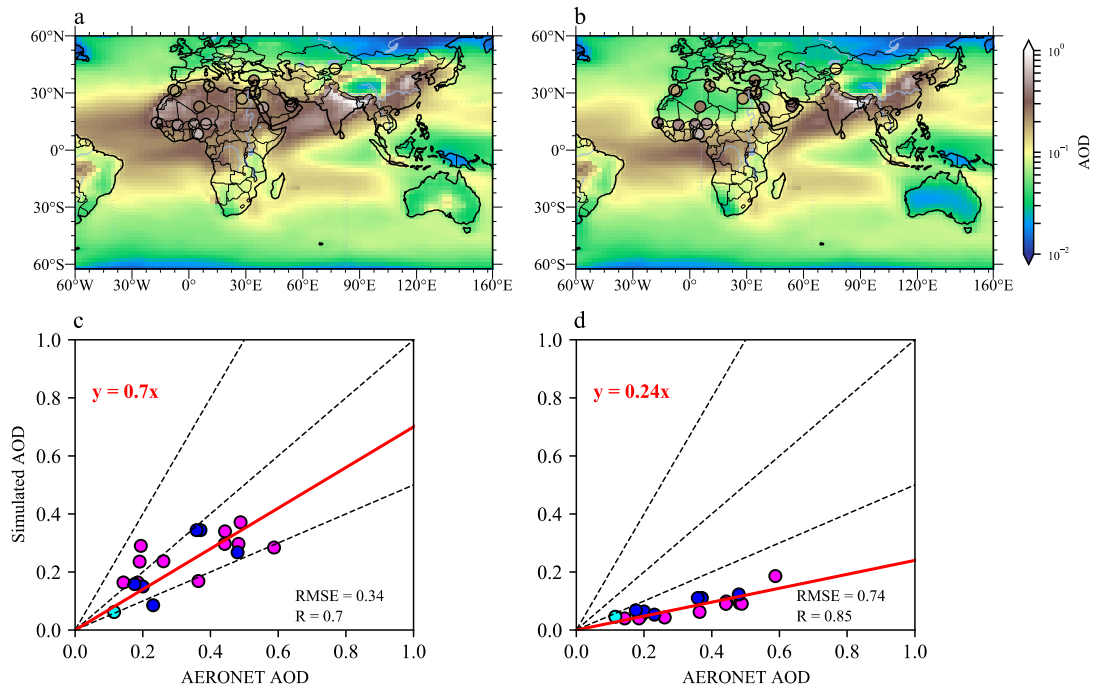
Figure 6. (a) Annual mean AOD at 532 nm wavelength from 2014 to 2018 simulated by
CESM1/CARMA, denoted by the color-filled contours; (b) same as (a) for simulation without dust.
The measured AOD from 18 AERONET ground sites located inside the major dust emission regions
(Figure 2) are denoted by the color-coded circles. (c) Comparison of the simulated annual mean AOD
at 532 nm wavelength with measurements from 2014 to 2018 for the most of the AERONET sites.
North Africa, the Middle East and Asia are represented as pink, cyan and blue number, respectively. (d)
same as (c) but for without dust. The solid red line denotes the best fit. The dashed black lines represent
1:2, 1:1, and 2:1 relationships between the observations and simulations.

4 Global distributions of North African, Middle Eastern, and Asian dust

In this section, we show the global distributions and source attributions of dust from the surface to the
lower stratosphere. Consistent with previous studies (Tanaka et al., 2006, Chin et al., 2007 and Kok et
al., 2021), modeled North African dust accounts for about 50-60% total global dust loading (mostly in
the lower troposphere). Validated by the recent global NASA ATom measurements, our study
calculated the dust source attributions in each altitude and the dust source attribution in the anticyclone
of the Asian summer monsoon region. We show that the Asian dust with less annual emission than the
North African dust is transported higher and become dominant in the upper troposphere and lower
stratosphere (UTLS).

4.1 Surface distribution of dust

Figure 7 shows the simulated annual mean surface concentrations of North African, Middle Eastern,

341 and Asian dust and their relative contributions to the simulated total dust from 2014 to 2018. In general,

342 the simulated maximum concentrations are located near the source regions. The dust concentrations

343 decrease dramatically by about two to three orders of magnitude from the source to remote regions due

344 to efficient dry and wet scavenging. Limited dust is transported across the equator from NH to SH

345 midlatitudes at the surface level. The simulated NH dust can travel to SH once convection lifts the dust

346 into the upper troposphere and lower stratosphere (Section 4.2).
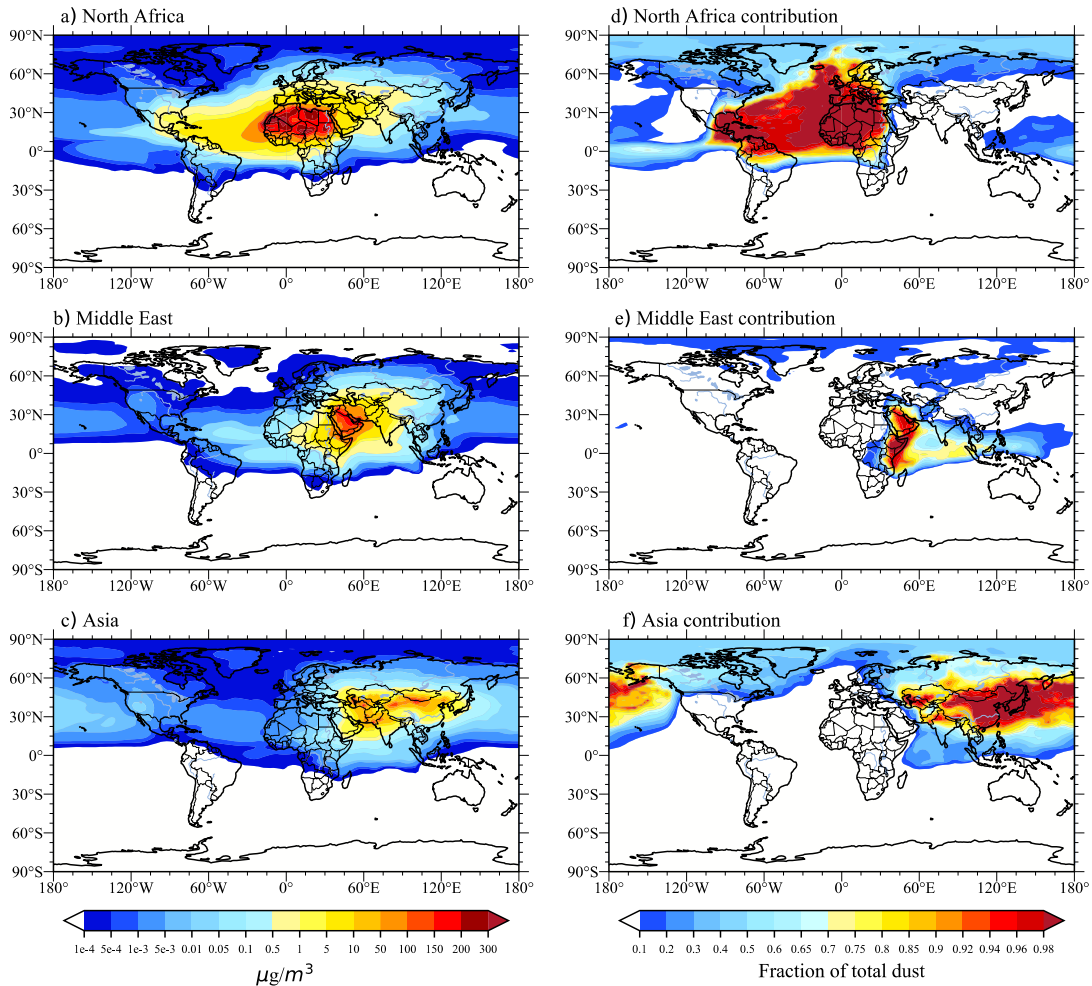
347

348 **Figure 7.** Simulated global spatial distribution of annual mean surface dust mass concentrations and

349 the fractional contribution of each source. Simulations are averaged from 2014 to 2018. Left panels

350 represent each source's concentration of dust. Right panels represent each source's contribution to total

351 dust.

352   North African dust dominates the surface dust concentrations in the Western Hemisphere

353 including the North Atlantic basin, Europe, Caribbean, and eastern North America. The model suggests

354 that simulated North African dust concentrations drop by three orders of magnitude during transport

355 from North Africa to 60 °N and peaks in the Caribbean. The modeled shape and direction of the

356 transported dust plume is similar to the simulations of Colarco et al. (2003). The trans-Atlantic

357 transport of the African dust to Amazon Basin in the northeasterly trade winds are observed (Yu et al.,

358 2015c; Swap et al., 1992; Prospero et al., 2014). Based on satellite and in-situ deposition data, Yu et al.

359 (2015c) quantified the deposition of African dust in the Amazon basin. Consistently, our simulated dust

360 over Amazon Basin is primarily transported from the North Africa.

361   The simulated annual mean dust concentration in Asia is about 24% of that in the North African,

362 which Su and Toon (2011) attribute to Asia having a much smaller area of dust sources than the Sahara.

363 Asian dust dominates in the Eastern Hemisphere including the North Pacific basin, Russia, and some

364 can be transported to Alaska and Canada. Previous studies have indicated that dust from the Gobi

365 Desert region entrained in a surface cyclone arrives in the western U.S. boundary layer via cross-

366 Pacific transport (Arimoto et al., 1996). With CARMA we show that although some Asian dust can be

367 transported to the western U.S. across the Pacific basin (Figure 7), its relative mass contribution to the

368 total dust concentration in the Western U.S. is about 1% on the annual basis (Figure 3). Simulated dust

369 in the boundary layer is mostly removed by wet and dry deposition during the cross-Pacific transport,

370 while lifted Asian dust can be transported more efficiently across the Pacific basin and accounts for

371 about 50% of the dust loading in the middle troposphere above the western U.S. (Figure S5). The

372 Pacific Dust Experiment (PACDEX) shows that the coarse mode Asian dust is rapidly removed amid

373 the remote transport, while the fine mode dust less than 2.5 um in diameter is entrained into the upper

374 air and transported across the Pacific Basin by the upper tropospheric westerly jets (Stith et al., 2009).

375 Consistent with PACDEX, our model shows that 92% of Asian dust mass that transported 10 km above

376 U.S. are less than 2.5 um in diameter (not shown). Middle Eastern dust contributes significantly to

377 surface dust loading over the Indian Ocean, eastern edge of Africa, southern India, and Southeast Asia.

378 The simulated latitudinal transport of Middle Eastern dust is limited (Figure S5). Our model suggests

379 that the contribution of North African and Asian dust to the surface dust in the Arctic is similar.

380 Significant contributions of Asian dust are confirmed through ice core isotopic analysis of the dust

381 deposited at the ice camp in Greenland (Bory et al., 2002; 2003). Note that the current model fails to

382 consider high-latitude dust sources in Siberia and Alaska, which are believed to be the major

383 contributors to Arctic dust (Lambert et al., 2015; Zwaaftink et al., 2016).

4.2 Vertical distribution of dust

Figure 8 compares the simulated vertical distributions of North African, Middle Eastern, and Asian dust in the lower, middle, and upper troposphere averaged from 2014 to 2018. Simulated global dust concentrations drop by one order of magnitude from the surface to about 600 hPa and by four orders of magnitude from the surface to 160 hPa. The rapid decline of dust mass concentration is due mostly to deposition and subgrid-scale convective removal above the cloud base (Yu et al., 2019; Froyd et al., 2022). However, Maloney et al. (2022) show that heterogenous nucleation of ice on dust, followed by sedimentation also contributes to loss of dust from the mid and upper troposphere. Model results show that the dust from the Sahara, Middle East, and Asia accounts for ~61.7%, 12.9%, and 13.9% of global annual mean surface dust concentration, respectively. In the NH midlatitudes, the relative contribution of Asian dust increases with altitude and becomes dominant in the upper troposphere. Asian dust contributes ~60.9% of the dust at pressures from 266 hPa to 160 hPa. Asian dust is mostly lifted in the spring by mid-latitude frontal systems (Caffrey et al., 2018). This higher relative contribution of Asian dust in the upper troposphere of the NH midlatitudes and tropics suggests that Asian dust is lifted more efficiently than North African dust. Asian dust is mostly lifted in mid-latitude springtime weather systems that are efficient at transporting dust aloft. North African dust is lifted in tropical systems that are less efficient at transporting dust to high altitudes since there is widespread descending air at the latitudes of the North African, which is in the descending branch of the Hadley circulation (Su and Toon, 2011). The upward transport of North African dust is restricted due to infrequent deep convection over the North African (Froyd et al., 2022). Frequent convective activity and cold frontal systems (Kawai et al., 2018, 2015; Hara et al., 2009) transport Asian dust upward to higher altitudes. Figures 8d-8e show that the upper tropospheric dust concentration in the NH midlatitudes is about one order of magnitude higher than that in the tropics. Note that the tropical dust in the middle and upper troposphere over the Pacific basin is overestimated by one order of magnitude compared with the Atom1 observation (Figure 5). However, model's performance on the tropical dust varies with seasons. For example, model underestimated the Atom3 observation by one-order of magnitude, while better agreements are made compared with Atom2 and Atom4 observations (Supplement figures S2-S4). In general, modeled annual mean distribution of tropical dust is subject to large uncertainties (in Figure 8). Especially the convective transport parameterization for a climate model with coarse resolution is

413 still highly uncertain.
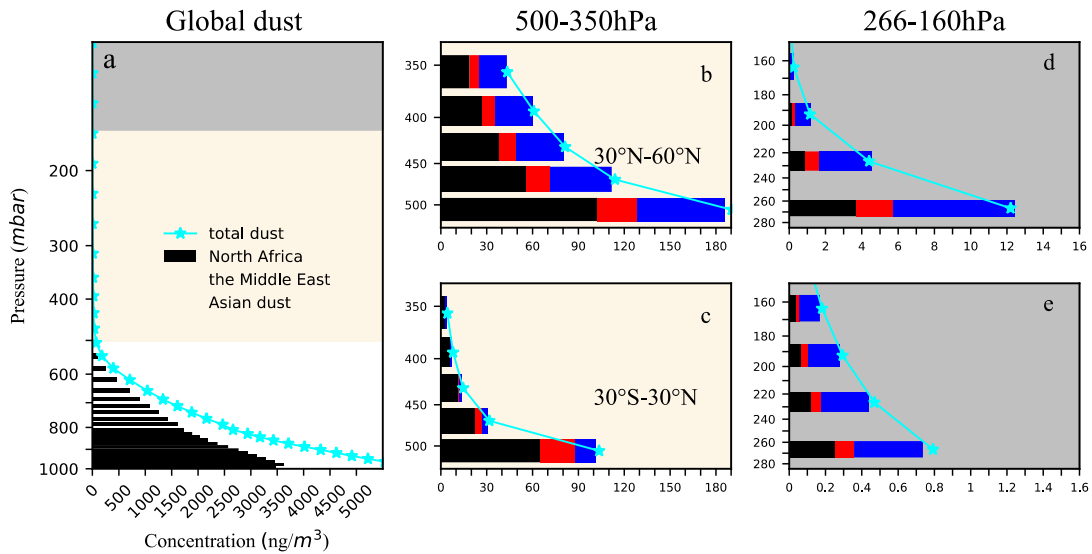
Figure 8. (a) Simulated vertical profiles of average dust concentration for 2014 to 2018 from each desert emission zone; green bars denote North African dust, red bars denote Middle Eastern dust, and blue bars denote Asian dust. (b-d) Same as Figure 8a but averaged for Northern Hemisphere (NH) midlatitudes (30°N-60°N) and tropics (30°S-30°N) from 500 to 350 hPa. (d-e) Same as Figure 8b-8c but for pressure levels from 266 to 160 hPa.

Figure 9 shows the vertical distribution of the zonal and annual mean dust fractional contributions from the three dust source regions. The Sahara dominates the tropical dust budget from the surface to the upper troposphere and accounts about 50% of dust in the troposphere of the NH mid-high latitudes. The model shows that limited North African dust is transported into the stratosphere. In contrast, Asian dust contributes less than North African dust in the troposphere except for the midlatitudes where the sources are located. Asian dust contributes more than 40% of the dust in the global UTLS, with the peak in the NH midlatitude UTLS having a mass fraction of more than 60%. Once the Asian dust is lifted high enough into the stratosphere, some can be transported to the SH UTLS. Our model suggests that Asian dust might be the dominant source of ice nucleating particles in the global UTLS. The simulations show that the fractional contribution of North African and Asian dust is comparable in the lower and middle troposphere of the Arctic.
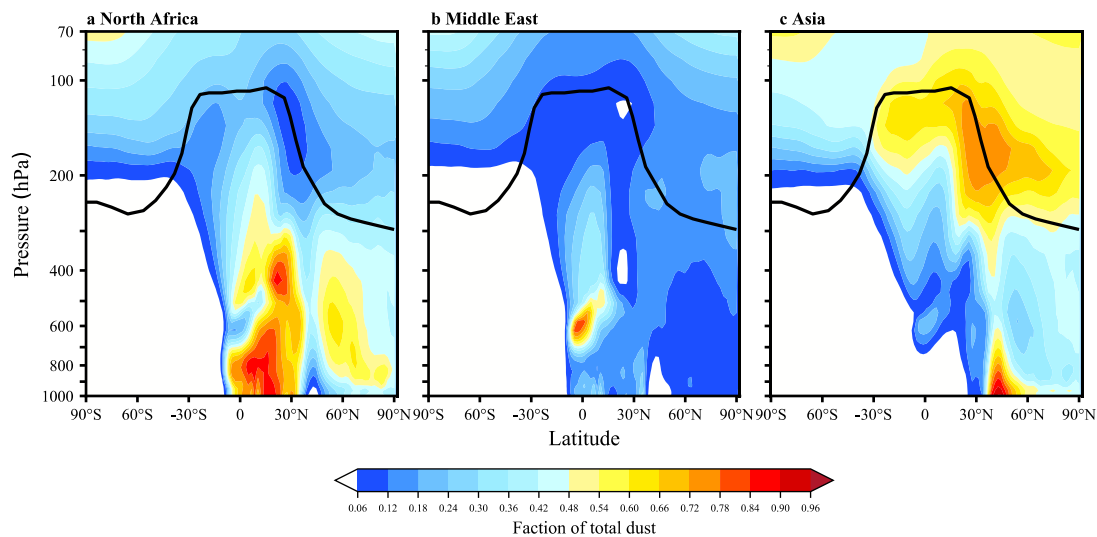
Figure 9. Simulation of each dust source's fractional contribution to zonal and annual average total dust as a function of altitude (left axis) and latitude (bottom axis). Shading indicates dust concentrations, and the black line in each figure denotes the annually averaged simulated tropopause height.

4.3 Dust attribution in the Asian summer monsoon region

A layer of aerosols in the UTLS of the ASM is revealed by satellites (Thomason and Vernier, 2013; Vernier et al., 2015; Vernier et al., 2011) and balloon-borne optical particle counters (Vernier et al., 2018; Yu et al., 2017). In the meantime, a high occurrence of cirrus clouds is found by satellites (Sassen et al., 2008; Nazaryan et al., 2008). The relative contributions of dust particles to the cirrus cloud in the ASM region remain unquantified and worth future evaluation. Recent airborne in-situ measurements suggest that the ASM tropopause aerosol layer is composed of mostly sulfate, organics, and nitrate (Hopfner et al., 2019; Appel et al., 2022). The budget of dust particles near the tropopause (~100 hPa) and at cirrus altitudes (e.g., 500-200 hPa) remains unquantified.

Figure 10 illustrates the simulated June-July-August (JJA) dust concentrations at 100 hPa averaged from 2014 to 2018. A peak of dust is simulated in the ASM region associated with the anticyclonic air flow similar to sulfate and organics. However, the dust abundance is extremely limited compared with sulfate and organics. The simulated mass fraction of aerosol contributed by dust is ~4% at 200 hPa and 0.08% at 100 hPa inside the ASM (Figure S6). As expected, Asian dust dominates the dust budget in the ASM region, with a relative contribution 1-2 orders of magnitude higher than North African and Middle Eastern dust. There is limited North African and Middle Eastern dust transport to

the ASM region by the strong upper tropospheric westerlies (Tanaka et al., 2005; Prasad and Singh,

2007). Note that the dust concentration simulated by CESM1/CARMA at 100 hPa in the ASM region is

about 9 x 10^{-5} µg/m^3, which is about 3 orders of magnitude smaller than the values simulated by the

CESM-MAM7 model reported by Bossolasco et al. (2021). Such low values of dust concentration are

due to inclusion of secondary activation of dust above the cloud base in the convective transport

scheme revised by Yu et al. (2019). Failure to include this removal will lead to large overestimates of

dust aloft.
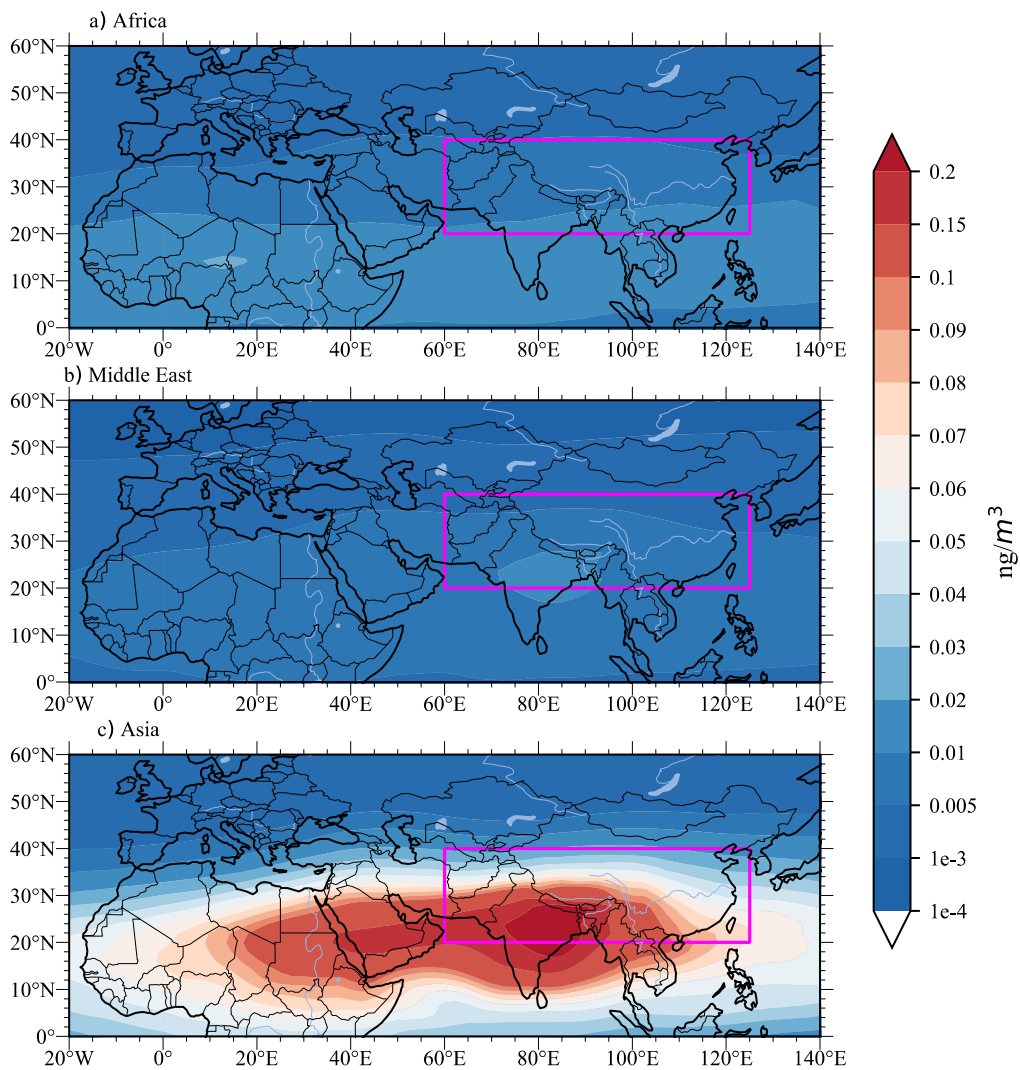
Figure 10. Simulated mass concentrations of North African, Middle East and Asian dust at 100 hPa
(left) averaged in June-July-August (JJA) from year 2014 to 2018. Purple boxes denote the Asian
Summer Monsoon region.

5 Summary

This study uses a sectional aerosol model coupled with a climate model, CESM1/CARMA, to simulate the global distribution of dust, 85% over which comes from Asian, Middle Eastern, and North African sources. Compared with measurements reported in Adebiyi and Kok (2020), the model of Yu et al. (2015b) underestimates the observed dust in the size range between 1 and 3 μm by one order of magnitude. We modified the size distribution of the dust emission, and the improved model is within the error bars of measurements summarized by Adebiyi and Kok (2020). Both observations and the simulations suggest that the dust mass size distribution increases by about 4 orders of magnitude from 0.1 μm to 2 μm, reaches its highest values around 2-3 micrometers in diameter and remains fairly constant for larger sizes up to 20 μm diameter. We compared the simulated dust distributions with multiple observational datasets including surface and airborne in-situ measurements over remote regions and aerosol optical depth measurements near the dust source regions. CESM1/CARMA reproduces the annual mean dust surface concentrations around the globe within one order of magnitude of the observations summarized in Huneeus et al. (2011). The global vertical distributions of dust measured by PALMS during the NASA ATom field campaign are used to constrain the model. Both the model and PALMS measurements suggest that dust mass concentrations over remote ocean basins drop by two to three orders of magnitude from the surface to the upper troposphere (200 hPa). Simulations show that about 52% of dust near the surface are coarse, while 95% of the total dust concentration in the upper troposphere is fine dust (with diameter less than 4.5 μm). The rapid decline of dust aerosols with altitude is associated with the efficient in-cloud convective removal of dust aerosols (Froyd et al., 2022; Yu et al., 2019). However, in situ cirrus formation can also lead to downward transport of dust (Maloney et al., 2022). In addition, both the model and PALMS measurements suggest that dust concentrations in the lower troposphere of the NH midlatitudes (27ºN-60ºN) and tropics (27ºS-27ºN) are about an order of magnitude higher than that in the SH midlatitudes (27ºS-60ºS). The model captures ~90% of the annual mean column aerosol optical depth measured by 33 AERONET stations near the dust source regions.

Our simulations suggest that the annual mean dust emissions from the Sahara, Middle East, and Asia account for ~59.7%, 12.5%, and 13.3% of global annual mean dust emissions, respectively. Dust emitted from the Sahara is transported toward Europe, but mostly to the Western Hemisphere including

492   the North Atlantic basin, and eastern North America. Asian dust dominates the Eastern Hemisphere

493   including the North Pacific basin, Russia, and some can be transported to Alaska and Canada. Middle

494   Eastern dust contributes significantly to the surface dust over the Indian Ocean, the eastern edge of

495   Africa, southern India, and Southeast Asia. Although North African dust dominates global dust mass

496   loading at the surface, the relative contribution of Asian dust increases with altitude and becomes

497   dominant in the upper troposphere of the northern hemisphere (NH). Once the Asian dust is lifted high

498   enough into the stratosphere, some can be transported to the SH UTLS. Asian dust might be the

499   dominant source of ice nucleating particles in the global UTLS. Asian dust contributes ~60.9% of the

500   dust mass at pressure levels from 266 hPa to 160 hPa. The increasing fractional contribution of Asian

501   dust is due to efficient vertical transport in midlatitude weather systems, while tropical weather systems

502   are not as efficient due to subsiding motion in the descending branch of the Hadley circulation and

503   convective activity over the Sahara is relatively infrequent (Froyd et al., 2022). Asian dust dominates

504   the dust budget in the global upper troposphere during the summer months, with the peak fractional

505   contribution in the ASM region, which is about 1-2 orders of magnitude higher than that of North

506   African and Middle Eastern dust. The model suggests that the dust forms a local maximum in the ASM

507   anticyclone as well as organics and nitrate (Yu et al., 2022). However, the simulated dust mass

508   concentration is only ~0.08% of the total aerosols in the Asian Tropopause Aerosol Layer (ATAL).

509   Constrained by the state-of-the-art measurements of dust at the global scale, our model highlights the

510   significant contribution of Asian dust to the global upper troposphere where cirrus clouds may form

511   heterogeneously.

512   *Data availability.* Dust surface measurements data are reported in Huneeus et al. (2011) and can be

513   found at https://aerocom-classic.met.no/DATA/download/DUST_BENCHMARK_HUNEEUS2011/;

514   NASA ATom data are available at https://espo.nasa.gov/atom/content/ATom; AERONET data can be

515   found http://aeronet.gsfc.nasa.gov/.

516

517   *Author contributions.* P.Y. designed the research and ran CESM1/CARMA model. S.L. analyzed the

518   model output, observational datasets and wrote the paper. L.Z, D.M.M, K.D.F and O.B.T provided

519   effective and constructive comments on the study. K.D.F and D.M.M provided the PLAMS datasets.

520   All authors edited the paper.

521

522   *Competing interests.* The authors declare no competing interests.

523

524   *Acknowledgements.* This work has been supported by the second Tibetan Plateau Scientific Expedition

525   and Research Program (2019QZKK0604); L.Z. is supported by Guangdong Innovative and

526   Entrepreneurial Research Team Program (2019ZT08G669); S.L. and P.Y. are partly supported by

527   National Natural Science Foundation of China (42175089, 42121004). OBT was supported by NSF

528   Award 1853932. Participation of PALMS in the ATom mission was supported by NOAA climate

529   funding and NASA award NNH15AB12I. We thank Charles A. Brock at NOAA for providing the

530   NASA ATom total aerosol size distribution data. The CESM project is supported by the National

531   Science Foundation and the Office of Science (BER) of the U.S. Department of Energy. We

532   acknowledge high-performance computing platform of Jinan University.

533

References

Adebiyi, A. A. and Kok, J. F.: Climate models miss most of the coarse dust in the atmosphere, Sci. Adv., 6, 10.1126/sciadv.aaz9507, 2020.

d'Almeida, G. A.: A model for Saharan dust transport, J. Appl. Meteorol. Climatol., 25, 903–916, 1986.

Andreae, M. O.: Climatic effects of changing atmospheric aerosol levels, World Surv. Climatol., 16, 347–398, 1995.

Andreae, M. O., Charlson, R. J., Bruynseels, F., Storms, H., Van Grieken, R., and Maenhaut, W.: Internal mixture of sea salt, silicates, and excess sulfate in marine aerosols, Science, 232, 1620–1623, 1986.

Appel, O., Köllner, F., Dragoneas, A., Hünig, A., Molleker, S., Schlager, H., Mahnke, C., Weigel, R., Port, M., and Schulz, C.: Chemical analysis of the Asian Tropopause Aerosol Layer (ATAL) with emphasis on secondary aerosol particles using aircraft based in situ aerosol mass spectrometry, Atmos. Chem. Phys. Discuss., 1–37, 2022.

Arimoto, R., Duce, R. A., Savoie, D. L., Prospero, J. M., Talbot, R., Cullen, J. D., Tomza, U., Lewis, N. F., and Ray, B. J.: Relationships among aerosol constituents from Asia and the North Pacific during PEM-West A, J. Geophys. Res. Atmospheres, 101, 2011–2023, https://doi.org/10.1029/95JD01071, 1996.

Balkanski, Y., Schulz, M., Claquin, T., and Guibert, S.: Reevaluation of Mineral aerosol radiative forcings suggests a better agreement with satellite and AERONET data, Atmos. Chem. Phys., 7, 81-95, 10.5194/acp-7-81-2007, 2007.

Bardeen, C., Toon, O., Jensen, E., Marsh, D., and Harvey, V.: Numerical simulations of the three-dimensional distribution of meteoric dust in the mesosphere and upper stratosphere, Journal of Geophysical Research: Atmospheres, 113, 2008.

Bory A J M, Biscaye P E, Svensson A, et al.: Seasonal variability in the origin of recent atmospheric mineral dust at NorthGRIP, Greenland, Earth and Planetary Science Letters, 196(3-4): 123-134, https://doi.org/10.1016/S0012-821X(01)00609-4, 2002.

Bory A J M, Biscaye P E, Grousset F E.: Two distinct seasonal Asian source regions for mineral dust deposited in Greenland (NorthGRIP), Geophys. Res. Lett., 30(4), https://doi.org/10.1029/2002GL016446, 2003.

Bossolasco, A., Jegou, F., Sellitto, P., Berthet, G., Kloss, C., and Legras, B.: Global modeling studies of composition and decadal trends of the Asian Tropopause Aerosol Layer, Atmos. Chem. Phys., 21, 2745-2764, doi: 10.5194/acp-21-2745-2021, 2021.

Bourgeois, I., Peischl, J., Thompson, C. R., Aikin, K. C., Campos, T., Clark, H., Commane, R., Daube, B., Diskin, G. W., Elkins, J. W., Gao, R.-S., Gaudel, A., Hintsa, E. J., Johnson, B. J., Kivi, R., McKain, K., Moore, F. L., Parrish, D. D., Querel, R., Ray, E., Sánchez, R., Sweeney, C., Tarasick, D. W., Thompson, A. M., Thouret, V., Witte, J. C., Wofsy, S. C., and Ryerson, T. B.: Global-scale distribution of ozone in the remote troposphere from the ATom and HIPPO airborne field missions, Atmos. Chem. Phys., 20, 10611–10635, doi: 10.5194/acp-20-10611-2020, 2020.

Bourgeois, Q., Ekman, A. M. L., and Krejci, R.: Aerosol transport over the Andes from the Amazon Basin to the remote Pacific Ocean: A multiyear CALIOP assessment, J. Geophys. Res. Atmos., 120, 8411-8425, doi: 10.1002/2015jd023254, 2015.

Brock, C. A., Williamson, C., Kupc, A., Froyd, K. D., Erdesz, F., Wagner, N., Richardson, M., Schwarz, J. P., Gao, R. S., Katich, J. M., Campuzano-Jost, P., Nault, B. A., Schroder, J. C., Jimenez, J. L., Weinzierl, B., Dollner, M., Bui, T., and Murphy, D. M.: Aerosol size distributions during the Atmospheric Tomography Mission (ATom): methods, uncertainties, and data products, Atmos. Meas.

578   Tech., 12, 3081-3099, doi: 10.5194/amt-12-3081-2019, 2019.

579   Caffrey, P. F., Fromm, M. D., and Kablick, G. P.: WRF-Chem Simulation of an East Asian Dust-Infused

580   Baroclinic Storm (DIBS), J. Geophys. Res. Atmos., 123, 6880-6895, 10.1029/2017jd027848, 2018.

581   Chin, M., Diehl, T., Ginoux, P., and Malm, W.: Intercontinental transport of pollution and dust aerosols:

582   implications for regional air quality: Atmos. Chem. Phys., 7, 5501-5517, 10.5194/acp-7-5501-2007,

583   2007.

584   Colarco P R, Toon O B, Reid J S, et al. North African dust transport to the Caribbean during PRIDE: 2.

585   Transport, vertical profiles, and deposition in simulations of in situ and remote sensing observations[J].

586   J. Geophys. Res. Atmos., 108, doi: 10.1029/2002JD002659, 2003.

587   Cziczo, D. J., Froyd, K. D., Hoose, C., Jensen, E. J., Diao, M. H., Zondlo, M. A., Smith, J. B., Twohy, C.

588   H., and Murphy, D. M.: Clarifying the Dominant Sources and Mechanisms of Cirrus Cloud Formation,

589   Science, 340, 1320-1324, doi: 10.1126/science.1234145, 2013.

590   Di Biagio, C., Formenti, P., Balkanski, Y., Caponi, L., Cazaunau, M., Pangui, E., Journet, E., Nowak, S.,

591   Andreae, M. O., Kandler, K., Saeed, T., Piketh, S., Seibert, D., Williams, E., and Doussin, J. F.:

592   Complex refractive indices and single-scattering albedo of global dust aerosols in the shortwave

593   spectrum and relationship to size and iron content: Atmos. Chem. Phys., 19, 15503-15531,

594   10.5194/acp-19-15503-2019, 2019.

595   Froyd, K. D., Murphy, D. M., Lawson, P., Baumgardner, D., and Herman, R. L.: Aerosols that form

596   subvisible cirrus at the tropical tropopause, Atmos. Chem. Phys., 10, 209-218, doi: 10.5194/acp-10-

597   209-2010, 2010.

598   Froyd, K. D., Murphy, D. M., Brock, C. A., Campuzano-Jost, P., Dibb, J. E., Jimenez, J. L., Kupc, A.,

599   Middlebrook, A. M., Schill, G. P., Thornhill, K. L., Williamson, C. J., Wilson, J. C., and Ziemba, L.

600   D.: A new method to quantify mineral dust and other aerosol species from aircraft platforms using

601   single-particle mass spectrometry, Atmos. Meas. Tech., 12, 6209-6239, doi: 10.5194/amt-12-6209-

602   2019, 2019.

603   Froyd, K. D., Yu, P. F., Schill, G. P., Brock, C. A., Kupc, A., Williamson, C. J., Jensen, E. J., Ray, E.,

604   Rosenlof, K. H., Bian, H. S., Darmenov, A. S., Colarco, P. R., Diskin, G. S., Bui, T., and Murphy, D.

605   M.: Dominant role of mineral dust in cirrus cloud formation revealed by global-scale measurements,

606   Nat. Geosci., 15, 177-+, doi: 10.1038/s41561-022-00901-w, 2022.

607   Ginoux, P., Chin, M., Tegen, I., Prospero, J. M., Holben, B., Dubovik, O., and Lin, S. J.: Sources and

608   distributions of dust aerosols simulated with the GOCART model, J. Geophys. Res. Atmos., 106,

609   20255-20273, doi: 10.1029/2000jd000053, 2001.

610   Grell, G. A. and Freitas, S. R.: A scale and aerosol aware stochastic convective parameterization for

611   weather and air quality modeling, Atmos. Chem. Phys., 14, 5233-5250, doi: 10.5194/acp-14-5233-

612   2014, 2014.

613   Hopfner, M., Ungermann, J., Borrmann, S., Wagner, R., Spang, R., Riese, M., Stiller, G., Appel, O.,

614   Batenburg, A. M., Bucci, S., Cairo, F., Dragoneas, A., Friedl-Vallon, F., Hunig, A., Johansson, S.,

615   Krasauskas, L., Legras, B., Leisner, T., Mahnke, C., Mohler, O., Molleker, S., Muller, R., Neubert, T.,

616   Orphal, J., Preusse, P., Rex, M., Saathoff, H., Stroh, F., Weigel, R., and Wohltmann, I.: Ammonium

617   nitrate particles formed in upper troposphere from ground ammonia sources during Asian monsoons,

618   Nat. Geosci., 12, 608-+, doi: 10.1038/s41561-019-0385-8, 2019.

619   Hara, Y., Yumimoto, K., Uno, I., Shimizu, A., Sugimoto, N., Liu, Z., and Winker, D.: Asian dust outflow

620   in the PBL and free atmosphere retrieved by NASA CALIPSO and an assimilated dust transport model,

621   Atmos. Chem. Phys., 9, 1227–1239, 2009.

Huneeus, N., Schulz, M., Balkanski, Y., Griesfeller, J., Prospero, J., Kinne, S., Bauer, S., Boucher, O., Chin, M., Dentener, F., Diehl, T., Easter, R., Fillmore, D., Ghan, S., Ginoux, P., Grini, A., Horowitz, L., Koch, D., Krol, M. C., Landing, W., Liu, X., Mahowald, N., Miller, R., Morcrette, J. J., Myhre, G., Penner, J., Perlwitz, J., Stier, P., Takemura, T., and Zender, C. S.: Global dust model intercomparison in AeroCom phase I, Atmos. Chem. Phys., 11, 7781-7816, doi: 10.5194/acp-11-7781-2011, 2011.

Karyampudi, V. M.: A detailed synoptic-scale study of the structure, dynamics, and radiative effects of the Saharan air layer over the eastern tropical Atlantic during the GARP Atlantic tropical experiment, 1979.

Karyampudi, V. M., Palm, S. P., Reagen, J. A., Fang, H., Grant, W. B., Hoff, R. M., Moulin, C., Pierce, H. F., Torres, O., Browell, E. V., and Melfi, S. H.: Validation of the Saharan Dust Plume Conceptual Model Using Lidar, Meteosat, and ECMWF Data, Bull. Am. Meteorol. Soc., 80, 1045–1076, doi: 10.1175/1520-0477(1999)080<1045:VOTSDP>2.0.CO;2, 1999.

Kawai, K., Kai, K., Jin, Y., Sugimoto, N., and Batdorj, D.: Dust Event in the Gobi Desert on 22-23 May 2013: Transport of Dust from the Atmospheric Boundary Layer to the Free Troposphere by a Cold Front, Sola, 11, 156-159, doi: 10.2151/sola.2015-035, 2015.

Kawai, K., Kai, K., Jin, Y., Sugimoto, N., and Batdorj, D.: Lidar Network Observation of Dust Layer Development over the Gobi Desert in Association with a Cold Frontal System on 22-23 May 2013, J. Meteorolog. Soc. Jpn., 96, 255-268, doi: 10.2151/jmsj.2018-023, 2018.

Kok, J. F.: A scaling theory for the size distribution of emitted dust aerosols suggests climate models underestimate the size of the global dust cycle: PNAS, 108, 1016-1021, 10.1073/pnas.1014798108, 2011.

Kok J. F., Adebiyi, A. A., Albani S., et al. : Contribution of the world's main dust source regions to the global cycle of desert dust, Atmos. Chem. Phys., 21, 8169-8193, doi: 10.5194/acp-21-8169-2021, 2021.

Levin, Z., Ganor, E., and Gladstein, V.: The Effects of Desert Particles Coated with Sulfate on Rain Formation in the Eastern Mediterranean, J. Appl. Meteorol. Climatol., 35, 1511–1523, doi:10.1175/1520-0450(1996)035<1511:TEODPC>2.0.CO;2, 1996.

Lambert, F., Tagliabue, A., Shaffer, G., Lamy, F., Winckler, G., Farias, L., Gallardo, L., and De Pol-Holz, R.: Dust fluxes and iron fertilization in Holocene and Last Glacial Maximum climates, Geophys. Res. Lett., 42, 6014-6023, doi: 10.1002/2015gl064250, 2015.

Ma, J. Z., Bruhl, C., He, Q. S., Steil, B., Karydis, V. A., Klingmuller, K., Tost, H., Chen, B., Jin, Y. F., Liu, N. W., Xu, X. D., Yan, P., Zhou, X. J., Abdelrahman, K., Pozzer, A., and Lelieveld, J.: Modeling the aerosol chemical composition of the tropopause over the Tibetan Plateau during the Asian summer monsoon: Atmos. Chem. Phys., 19, 11587-11612, 10.5194/acp-19-11587-2019, 2019.

Mahowald, N. M., Baker, A. R., Bergametti, G., Brooks, N., Duce, R. A., Jickells, T. D., Kubilay, N., Prospero, J. M., and Tegen, I.: Atmospheric global dust cycle and iron inputs to the ocean, Global Biogeochem. Cy., 19(4), GB4025, doi:10.1029/2004GB002402, 2005.

Mahowald, N., Jickells, T. D., Baker, A. R., Artaxo, P., BenitezNelson, C. R., Bergametti, G., Bond, T. C., Chen, Y., Cohen,D. D., Herut, B., Kubilay, N., Losno, R., Luo, C., Maenhaut,W., McGee, K. A., Okin, G. S., Siefert, R. L., and Tsukuda, S.:Global distribution of atmospheric phosphorus sources, concentrations and deposition rates, and anthropogenic impacts, Global Biogeochem. Cy., 22(4), GB4026, doi:10.1029/2008GB003240, 2008.

Mahowald, N. M., Engelstaedter, S., Luo, C., Sealy, A., Artaxo, P., Benitez-Nelson, C., Bonnet, S., Chen, Y., Chuang, P. Y., Cohen, D. D., Dulac, F., Herut, B., Johansen, A. M., Kubilay, N., Losno, R., Maenhaut, W., Paytan, A., Prospero, J. A., Shank, L. M., and Siefert, R. L.: Atmospheric Iron

Deposition: Global Distribution, Variability, and Human Perturbations, Annual Review of Marine Science, 1, 245-278, doi: 10.1146/annurev.marine.010908.163727, 2009.

Maloney, C., Toon, B., Bardeen, C., Yu, P. F., Froyd, K., Kay, J., and Woods, S.: The Balance Between Heterogeneous and Homogeneous Nucleation of Ice Clouds Using CAM5/CARMA, J. Geophys. Res. Atmos., 127, doi: 10.1029/2021jd035540, 2022.

Marticorena, B. and Bergametti, G.: Modeling the atmospheric dust cycle: 1. Design of a soil-derived dust emission scheme, J. Geophys. Res. Atmos., 100, 16415–16430, 1995.

Murphy, D. M., Middlebrook, A. M., and Warshawsky, M.: Cluster analysis of data from the Particle Analysis by Laser Mass Spectrometry (PALMS) instrument, Aerosol Science and Technology, 37, 382-391, doi: 10.1080/02786820300971, 2003.

Murphy, D. M., Cziczo, D. J., Froyd, K. D., Hudson, P. K., Matthew, B. M., Middlebrook, A. M., Peltier, R. E., Sullivan, A., Thomson, D. S., and Weber, R. J.: Single-particle mass spectrometry of tropospheric aerosol particles, J. Geophys. Res. Atmos., 111, doi: 10.1029/2006jd007340, 2006.

Murphy, D. M., Froyd, K. D., Bourgeois, I., Brock, C. A., Kupc, A., Peischl, J., Schill, G. P., Thompson, C. R., Williamson, C. J., and Yu, P. F.: Radiative and chemical implications of the size and composition of aerosol particles in the existing or modified global stratosphere, Atmos. Chem. Phys., 21, 8915-8932, doi: 10.5194/acp-21-8915-2021, 2021.

Nazaryan, H., McCormick, M. P., and Menzel, W. P.: Global characterization of cirrus clouds using CALIPSO data, Journal of Geophysical Research-Atmospheres, 113, doi: 10.1029/2007jd009481, 2008.

Prasad, A. K. and Singh, R. P.: Changes in aerosol parameters during major dust storm events (2001-2005) over the Indo-Gangetic Plains using AERONET and MODIS data, J. Geophys. Res. Atmos., 112, doi: 10.1029/2006jd007778, 2007.

Prospero, J. M.: Mineral aerosol transport to the Pacific Ocean, Chem. Oceanogr., 10, 188–218, 1989.

Prospero, J. M.: The atmospheric transport of particles to the ocean, Part. Flux Ocean, 57, 19–52, 1996.

Prospero, J. M. and Bonatti, E.: Continental dust in the atmosphere of the Eastern Equatorial Pacific, J. Geophys. Res., 74, 3362–3371, https://doi.org/10.1029/JC074i013p03362, 1969.

Prospero, J. M., F.-X. Collard, J. Molinie, and A. Jeannot: Characterizing the annual cycle of African dust transport to the Caribbean Basin and South America and its impact on air quality and the environment, Global Biogeochem. Cycles, 29, 757–773, doi:10.1002/2013GB004802, 2014.

Rosenfeld, D., Rudich, Y., and Lahav, R.: Desert dust suppressing precipitation: A possible desertification feedback loop, Proceedings of the National Academy of Sciences of the United States of America, 98, 5975-5980, doi: 10.1073/pnas.101122798, 2001.

Sassen, K., Wang, Z., and Liu, D.: Global distribution of cirrus clouds from CloudSat/Cloud-Aerosol Lidar and Infrared Pathfinder Satellite Observations (CALIPSO) measurements, J. Geophys. Res. Atmos., 113, doi: 10.1029/2008jd009972, 2008.

Satheesh, S. K. and Moorthy, K. K.: Radiative effects of natural aerosols: A review, Atmos. Environ., 39, 2089-2110, 10.1016/j.atmosenv.2004.12.029, 2005.

Sinyuk, A., Torres, O., and Dubovik, O.: Combined use of satellite and surface observations to infer the imaginary part of refractive index of Saharan dust: Geophys. Res. Lett., 30, 10.1029/2002gl016189, 2003.

Sokolik, I. N. and Toon, O. B.: Direct radiative forcing by anthropogenic airborne mineral aerosols, Nature, 381, 681-683, 10.1038/381681a0, 1996.

Sokolik, I. N. and Toon, O. B.: Incorporation of mineralogical composition into models of the radiative

properties of mineral aerosol from UV to IR wavelengths, J. Geophys. Res. Atmos., 104, 9423–9444, 1999.

Spanu, A., Dollner, M., Gasteiger, J., Bui, T. P., and Weinzierl, B.: Flow-induced errors in airborne in situ measurements of aerosols and clouds, Atmos. Meas. Tech., 13, 1963-1987, doi: 10.5194/amt-13-1963-2020, 2020.

Stith, J. L., Ramanathan, V., Cooper, W. A., Roberts, G. C., DeMott, P. J., Carmichael, G., Hatch, C. D., Adhikary, B., Twohy, C. H., Rogers, D. C., Baumgardner, D., Prenni, A. J., Campos, T., Gao, R., Anderson, J., and Feng, Y.: An overview of aircraft observations from the Pacific Dust Experiment campaign, J. Geophys. Res. Atmos., 114, doi: 10.1029/2008jd010924, 2009.

Su, L. and Toon, O. B.: Numerical simulations of Asian dust storms using a coupled climate-aerosol microphysical model, J. Geophys. Res. Atmos., 114, doi: 10.1029/2008jd010956, 2009.

Su, L. and Toon, O. B.: Saharan and Asian dust: similarities and differences determined by CALIPSO, AERONET, and a coupled climate-aerosol microphysical model, Atmos. Chem. Phys., 11, 3263-3280, doi: 10.5194/acp-11-3263-2011, 2011.

Swap R, Garstang M, Greco S, et al.: Saharan dust in the Amazon Basin, Tellus B, 44(2): 133-149, https://doi.org/10.1034/j.1600-0889.1992.t01-1-00005.x, 1992,.

Tanaka, T. Y., Kurosaki, Y., Chiba, M., Matsumura, T., Nagai, T., Yamazaki, A., Uchiyama, A., Tsunematsu, N., and Kai, K.: Possible transcontinental dust transport from North Africa and the Middle East to East Asia, Atmos. Environ., 39, 3901–3909, doi: 10.1016/j.atmosenv.2005.03.034, 2005.

Tanaka, T. Y. and Chiba, M.: A numerical study of the contributions of dust source regions to the global dust budget: Global Planet. Change, 52, 88-104, 10.1016/j.gloplacha.2006.02.002, 2006.

Tegen, I. and Lacis, A. A.: Modeling of particle size distribution and its influence on the radiative properties of mineral dust aerosol, J. Geophys. Res. Atmos., 101, 19237-19244, 10.1029/95jd03610, 1996.

Tegen, I.: Modeling the mineral dust aerosol cycle in the climate system: Quat. Sci. Rev., 22, 1821-1834, 10.1016/s0277-3791(03)00163-x, 2003.

Tegen, I. and Schepanski, K.: The global distribution of mineral dust, IOP Conf. Ser. Earth Environ. Sci., 7, 012001, doi: 10.1088/1755-1307/7/1/012001, 2009.

Textor, C., Schulz, M., Guibert, S., Kinne, S., Balkanski, Y., Bauer, S., Berntsen, T., Berglen, T., Boucher, O., Chin, M., Dentener, F., Diehl, T., Easter, R., Feichter, H., Fillmore, D., Ghan, S., Ginoux, P., Gong, S., Kristjansson, J. E., Krol, M., Lauer, A., Lamarque, J. F., Liu, X., Montanaro, V., Myhre, G., Penner, J., Pitari, G., Reddy, S., Seland, O., Stier, P., Takemura, T., and Tie, X.: Analysis and quantification of the diversities of aerosol life cycles within AeroCom, Atmos. Chem. Phys., 6, 1777-1813, doi: 10.5194/acp-6-1777-2006, 2006.

Thomason, L. W. and Vernier, J. P.: Improved SAGE II cloud/aerosol categorization and observations of the Asian tropopause aerosol layer: 1989-2005, Atmos. Chem. Phys., 13, 4605-4616, doi: 10.5194/acp-13-4605-2013, 2013.

Toon, O. B., Turco, R. P., Westphal, D., Malone, R., and Liu, M.: A Multidimensional Model for Aerosols: Description of Computational Analogs, J. Atmospheric Sci., 45, 2123–2144, doi: 10.1175/1520-0469(1988)045<2123:AMMFAD>2.0.CO;2, 1988.

Vernier, J. P., Thomason, L. W., and Kar, J.: CALIPSO detection of an Asian tropopause aerosol layer, Geophys. Res. Lett., 38, doi: 10.1029/2010gl046614, 2011.

Vernier, J. P., Fairlie, T. D., Natarajan, M., Wienhold, F. G., Bian, J., Martinsson, B. G., Crumeyrolle, S., Thomason, L. W., and Bedka, K. M.: Increase in upper tropospheric and lower stratospheric aerosol

levels and its potential connection with Asian pollution, J. Geophys. Res. Atmos., 120, 1608-1619, doi: 10.1002/2014jd022372, 2015.

Vernier, J. P., Fairlie, T. D., Deshler, T., Ratnam, M. V., Gadhavi, H., Kumar, B. S., Natarajan, M., Pandit, A. K., Raj, S. T. A., Kumar, A. H., Jayaraman, A., Singh, A. K., Rastogi, N., Sinha, P. R., Kumar, S., Tiwari, S., Wegner, T., Baker, N., Vignelles, D., Stenchikov, G., Shevchenko, I., Smith, J., Bedka, K., Kesarkar, A., Singh, V., Bhate, J., Ravikiran, V., Rao, M. D., Ravindrababu, S., Patel, A., Vernier, H., Wienhold, F. G., Liu, H., Knepppp, T. N., Thomason, L., Crawford, J., Ziembmba, L., Moore, J., Crumeyrolle, S., Williamson, M., Berthet, G., Jegou, F., and Renard, J. B.: BATAL The Balloon Measurement Campaigns of the Asian Tropopause Aerosol Layer, Bull. Am. Meteorol. Soc., 99, 955-973, doi: 10.1175/bams-d-17-0014.1, 2018.

Wang, H., Easter, R. C., Rasch, P. J., Wang, M., Liu, X., Ghan, S. J., Qian, Y., Yoon, J. H., Ma, P. L., and Vinoj, V.: Sensitivity of remote aerosol distributions to representation of cloud-aerosol interactions in a global climate model, Geosci. Model Dev., 6, 765-782, doi: 10.5194/gmd-6-765-2013, 2013.

Wang, R., Balkanski, Y., Boucher, O., Bopp, L., Chappell, A., Ciais, P., Hauglustaine, D., Penuelas, J., and Tao, S.: Sources, transport and deposition of iron in the global atmosphere: Atmos. Chem. Phys., 15, 6247-6270, 10.5194/acp-15-6247-2015, 2015.

Wofsy, S. C., Afshar, S., Allen, H. M., Apel, E. C., Asher, E. C., Barletta, B., Bent, J., Bian, H., Biggs, B. C., Blake, D. R., Blake, N., Bourgeois, I., Brock, C. A., Brune, W. H., Budney, J. W., Bui, T. P., Butler, A., Campuzano-Jost, P., Chang, C. S., Chin, M., Commane, R., Correa, G., Crounse, J. D., Cullis, P. D., Daube, B. C., Day, D. A., Dean-Day, J. M., Dibb, J. E., Digangi, J. P., Diskin, G. S., Dollner, M., Elkins, J. W., Erdesz, F., Fiore, A. M., Flynn, C. M., Froyd, K. D., Gesler, D. W., Hall, S. R., Hanisco, T. F., Hannun, R. A., Hills, A. J., Hintsa, E. J., Hoffman, A., Hornbrook, R. S., Huey, L. G., Hughes, S., Jimenez, J. L., Johnson, B. J., Katich, J. M., Keeling, R. F., Kim, M. J., Kupc, A., Lait, L. R., Lamarque, J.-F., Liu, J., Mckain, K., Mclaughlin, R. J., Meinardi, S., Miller, D. O., Montzka, S. A., Moore, F. L., Morgan, E. J., Murphy, D. M., Murray, L. T., Nault, B. A., Neuman, J. A., Newman, P. A., Nicely, J. M., Pan, X., Paplawsky, W., Peischl, J., Prather, M. J., Price, D. J., Ray, E. A., Reeves, J. M., Richardson, M., Rollins, A. W., Rosenlof, K. H., Ryerson, T. B., Scheuer, E., Schill, G. P., Schroder, J. C., Schwarz, J. P., St. Clair, J. M., Steenrod, S. D., Stephens, B. B., Strode, S. A., Sweeney, C., Tanner, D., Teng, A. P., Thames, A. B., Thompson, C. R., Ullmann, K., Veres, P. R., Vizenor, N., Wagner, N. L., Watt, A., Weber, R., Weinzierl, B. B., et al.: ATom: Merged Atmospheric Chemistry, Trace Gases, and Aerosols, ORNL DAAC, doi: 10.3334/ORNLDAAC/1581, 2018.

Wu, C., Lin, Z., Liu, X. : The global dust cycle and uncertainty in CMIP5 (Coupled Model Intercomparison Project phase 5) models, Atmos. Chem. Phys., 20, 10401-10425, doi: 10.5194/acp-20-10401-2020, 2020.

Yang, K., Wang, Z. E., Luo, T., Liu, X. H., and Wu, M. X.: Upper troposphere dust belt formation processes vary seasonally and spatially in the Northern Hemisphere, Communications Earth & Environment, 3, doi: 10.1038/s43247-022-00353-5, 2022.

Yu, H. B., Chin, M., Winker, D. M., Omar, A. H., Liu, Z. Y., Kittaka, C., and Diehl, T.: Global view of aerosol vertical distributions from CALIPSO lidar measurements and GOCART simulations: Regional and seasonal variations, J. Geophys. Res. Atmos., 115, doi: 10.1029/2009jd013364, 2010.

Yu, H. B., Chin, M., Bian, H. S., Yuan, T. L., Prospero, J. M., Omar, A. H., Remer, L. A., Winker, D. M., Yang, Y. K., Zhang, Y., and Zhang, Z. B.: Quantification of trans-Atlantic dust transport from seven-year (2007-2013) record of CALIPSO lidar measurements, Remote Sens. Environ., 159, 232-249, doi: 10.1016/j.rse.2014.12.010, 2015a.

Yu, P. F., Toon, O. B., Bardeen, C. G., Mills, M. J., Fan, T. Y., English, J. M., and Neely, R. R.: Evaluations of tropospheric aerosol properties simulated by the community earth system model with a sectional aerosol microphysics scheme, J. Adv. Model. Earth Syst., 7, 865-914, doi: 10.1002/2014ms000421, 2015b.

Yu, H. B., Chin, M., Yuan, T. L., Bian, H. S., Remer, L. A., Prospero, J. M., Omar, A., Winker, D., Yang, Y. K., Zhang, Y., Zhang, Z. B., and Zhao, C.: The fertilizing role of African dust in the Amazon rainforest: A first multiyear assessment based on data from Cloud-Aerosol Lidar and Infrared Pathfinder Satellite Observations: Geophys. Res. Lett., 42, 1984-1991, 10.1002/2015gl063040, 2015c.

Yu, P., Rosenlof, K. H., Liu, S., Telg, H., Thornberry, T. D., Rollins, A. W., Portmann, R. W., Bai, Z., Ray, E. A., Duan, Y., Pan, L. L., Toon, O. B., Bian, J., and Gao, R.-S.: Efficient transport of tropospheric aerosol into the stratosphere via the Asian summer monsoon anticyclone, Proc. Natl. Acad. Sci., 114, 6972–6977, doi: 10.1073/pnas.1701170114, 2017.

Yu, P. F., Froyd, K. D., Portmann, R. W., Toon, O. B., Freitas, S. R., Bardeen, C. G., Brock, C., Fan, T. Y., Gao, R. S., Katich, J. M., Kupc, A., Liu, S., Maloney, C., Murphy, D. M., Rosenlof, K. H., Schill, G., Schwarz, J. P., and Williamson, C.: Efficient In-Cloud Removal of Aerosols by Deep Convection, Geophys. Res. Lett., 46, 1061-1069, doi: 10.1029/2018gl080544, 2019.

Yu P, Lian S, Zhu Y, et al.: Abundant Nitrate and Nitric Acid Aerosol in the Upper troposphere and Lower Stratosphere: Geophys. Res. Lett., https://doi.org/10.1029/2022GL1002582022, 2022.

Zwaaftink, C. D. G., Grythe, H., Skov, H., and Stohl, A.: Substantial contribution of northern high-latitude sources to mineral dust in the Arctic, J. Geophys. Res. Atmos., 121, 13678-13697, doi: 10.1002/2016jd025482, 2016.